

A fully resolved smoothed particle hydrodynamics-discrete element method study of the rheology of suspensions: The role of inertia and grain shape

Cite as: Phys. Fluids **35**, 083325 (2023); doi: 10.1063/5.0161344

Submitted: 9 June 2023 · Accepted: 5 August 2023 ·

Published Online: 22 August 2023







View Online



Export Citation



CrossMark

Y. T. Li (李月婷),¹  N. Guo (郭宁),^{1,a)}  Z. X. Yang (杨仲轩),¹  and J. D. Zhao (赵吉东)² 

AFFILIATIONS

¹Computing Center for Geotechnical Engineering, Engineering Research Center of Urban Underground Space Development of Zhejiang Province, Department of Civil Engineering, Zhejiang University, Hangzhou 310058, China

²Department of Civil and Environmental Engineering, The Hong Kong University of Science and Technology, Clearwater Bay, Kowloon, Hong Kong

^{a)}Author to whom correspondence should be addressed: nguo@zju.edu.cn

ABSTRACT

This paper presents a numerical study on suspensions of monodisperse non-Brownian grains in a Couette flow. The fully resolved coupled smoothed particle hydrodynamics and discrete element method is employed to model the motion of arbitrarily shaped grains in a viscous fluid. The numerical method is benchmarked against its capability in accurately handling grain–fluid hydrodynamics and inter-grain collisions. It is then used to simulate suspension flows of varying particle Reynolds and Bagnold numbers subjected to different shear rates, solid concentrations, and solid-to-fluid density ratios. A special focus is placed on the effect of grain shape with different aspect ratios and convexities on the flow behavior. Both the inertia and the grain shape are found to affect the grain–fluid and inter-grain interactions and uniquely contribute to the overall shear stress and the rheology of the suspension. The local profiles of solid concentration suggest the presence of grain layering near the boundary walls, which becomes more pronounced with higher solid concentration and inertia, and increased non-circularity in grain shape. A further examination of the pair distribution function and average particle rotation reveals a strong correlation between suspension viscosity and grain microstructure and kinematics.

Published under an exclusive license by AIP Publishing. <https://doi.org/10.1063/5.0161344>

I. INTRODUCTION

Suspensions of solid grains in a fluid are prevalent in industrial processes, including paints, food processing, waste disposal, and fresh concrete, and present in natural occurring processes such as lavas, mudflows, and gravity currents. The interactions between solid grains and fluids are frequently diverse and complex, involving viscous shear, turbulence, solid–fluid hydrodynamics, and inter-grain contacts. Indeed, suspension flows remain one of the challenging flow patterns that are not fully understood.

Dimensionless numbers have been defined to characterize the flow regime of non-Brownian suspensions. Popular ones include the particle Reynolds number (Re_p) and the Bagnold number (B_a).¹ Most existing numerical studies on suspensions have focused on the limiting case at vanishing Reynolds number using algorithms such as Stokesian dynamics.^{2–5} Key findings from these studies include the microstructural anisotropy of grain pair distribution. It is supposed to be a major contributor to the non-Newtonian behavior of suspensions, often resulting in shear-thickening.⁶

Among recent advancements in numerical methods, direct numerical simulation (DNS) has become prevailing for simulating suspensions, e.g., using the Lattice-Boltzmann method (LBM),^{7–13} the immersed boundary method (IBM),^{14,15} and the fictitious domain method (FDM).^{16–19} These methods are suitable for analyzing inertial flows, arbitrarily shaped grains, and non-Newtonian fluids. Focusing on the weak inertia case, Patankar and Hu²⁰ investigated the effect of finite Re_p on the rheology of a dilute suspension of neutrally buoyant circular grains and attributed shear-thickening to the slower normalized angular velocity of grains as the Reynolds number increases. Kulkarni and Morris²¹ found that inertia magnifies the microstructural anisotropy and increases the grains' contribution to the effective viscosity. To assess the significance of inter-grain interactions and inertia of fluid and grains, Haddadi and Morris¹⁰ computed different stress mechanisms, and Rahmani *et al.*¹⁸ examined momentum balance in the fluid and solid phases for different flow regimes. Nevertheless, there remains limited understanding toward the

influence of enhanced inertia related to grains heavier than the fluid. Zhou and Prosperetti²² compared the results of solid-to-fluid density ratios between 2.5 and 10 at $Re_p = 20$ and 40 and found that an increased density ratio results in stronger and more frequent collisions between grains, leading to notable modifications in the grain distribution, velocity profile, and bulk stress.

Moreover, studies on suspensions of non-spherical grains are relatively scarce, mainly due to the difficulty of dealing with geometrically complex boundaries. Among non-spherical grain suspensions, fiber suspensions are the most extensively studied due to their wide industrial applications and the availability of simulation methods, such as slender body dynamics.^{23,24} Apart from slender grains, much of the literature on non-spherical grains in dense suspensions has focused on interactions dominated by inter-grain contacts. For example, the gear-like²⁵ and ellipsoidal²⁶ grains have been simulated using the discrete element method (DEM) considering short-range repulsive contact forces. However, even though collisional interaction is rare in dilute regimes, Daghooghi and Borazjani²⁷ have shown that there are still differences in rheology between suspensions of irregular-shaped and simple-shaped grains.

Considering the apparent gap in the literature as summarized above, the aim of this paper is to investigate the role of inertia and grain shape on the rheology of suspensions. Specifically, the contributions of fluid, grain–fluid hydrodynamics, and inter-grain collisional contacts to the effective viscosity will be analyzed for suspensions of grains with varying aspect ratios and convexities. The smoothed particle hydrodynamics (SPH) method is employed to simulate the fluid flow,^{28,29} and the DEM is used for the modeling of rigid grains. The interaction between the fluid and solid phases is considered through the fully resolved coupling between the two methods, which has been implemented in the high-performance open-source code DualSPHysics based on the work by Canelas *et al.*³⁰ The model has advantages in dealing with suspensions of complex-shaped grains within a unified meshless framework. Compared to Canelas *et al.*,³⁰ further improvement in calculating the tangential contact forces has been made in this study so that the model can be applicable to relatively dense suspensions with persistent inter-grain contacts.

The remainder of this paper is organized as follows: Section II details the methodology with formulations of the SPH and DEM and their coupling strategy. In Sec. III, the method is validated through five benchmark tests, including the water entry of a single disk, sedimentation of an ellipse, periodic flow around a sunflower-shaped object, pair-disk trajectories in a shear flow, and settlement of two disks exhibiting the drafting-kissing-tumbling phenomenon. Section IV analyzes the role of inertia and grain shape on the rheology of suspensions, in terms of effective viscosity, stress contributions, flow profile, pair microstructure, and grain rotation. Finally, Sec. V concludes the main findings of the study.

II. METHODOLOGY

A. SPH discretization

SPH is employed to discretize the problem domain using a set of smoothed particles that carry the information of field variables (e.g., mass, density, pressure, and velocity) and their gradients. The particles interact with their neighbors and move according to the governing equation. The integral representation of an arbitrary function $f(\mathbf{x}_i)$ at

point \mathbf{x}_i is approximated from the contributions of neighboring particles through the weighted kernel function W

$$f(\mathbf{x}_i) = \int_{\Omega} f(\mathbf{x}_j) W(|\mathbf{x}_i - \mathbf{x}_j|, h) dV \approx \sum_j f(\mathbf{x}_j) W(|\mathbf{x}_i - \mathbf{x}_j|, h) V_j, \quad (1)$$

where h is a smoothing length defining the kernel's influence size and taken as approximately $1.7d_p$ with d_p being the initial particle spacing in the study and V_j is the volume occupied by particle at \mathbf{x}_j . The Wendland kernel is used in this study,³¹

$$W(|\mathbf{x}_i - \mathbf{x}_j|, h) = \begin{cases} \alpha_D \left(1 - \frac{|\mathbf{x}_i - \mathbf{x}_j|}{2h}\right)^4 \left(\frac{2|\mathbf{x}_i - \mathbf{x}_j|}{h} + 1\right), & \frac{|\mathbf{x}_i - \mathbf{x}_j|}{h} \leq 2 \\ 0, & \text{otherwise,} \end{cases} \quad (2)$$

where $\alpha_D = 7/(4\pi h^2)$ for 2D cases and $21/(16\pi h^3)$ for 3D cases.

The discretized momentum conservation equation is written as

$$\begin{aligned} \frac{d\mathbf{v}_i}{dt} = & - \sum_j m_j \left(\frac{p_i + p_j}{\rho_i \cdot \rho_j} \right) \nabla_i W \\ & + \sum_j m_j \frac{4\nu_0(\mathbf{x}_i - \mathbf{x}_j) \cdot \nabla_i W}{(\rho_i + \rho_j)(|\mathbf{x}_i - \mathbf{x}_j|^2 + 0.01h^2)} (\mathbf{v}_i - \mathbf{v}_j) \\ & + \sum_j m_j \left(\frac{\boldsymbol{\tau}_i^s}{\rho_i^2} + \frac{\boldsymbol{\tau}_j^s}{\rho_j^2} \right) \cdot \nabla_i W + \mathbf{g}. \end{aligned} \quad (3)$$

The first term on the right-hand side of Eq. (3) is a symmetric balanced form of the pressure term³² where ρ_{\blacksquare} , m_{\blacksquare} , and p_{\blacksquare} ($\blacksquare = i$ or j) denote the particle density, mass, and pressure, respectively. $\nabla_i W$ is the gradient of kernel function with respect to \mathbf{x}_i . The second and third terms represent the viscous stress³³ and sub-particle-scale (SPS) stress,³⁴ respectively, where ν_0 is the fluid kinematic viscosity and $\boldsymbol{\tau}_{\blacksquare}^s$ is the SPS stress tensor, which introduces the effect of turbulent motion at smaller scales than the kernel scale. \mathbf{g} is the gravitational acceleration.

To avoid solving the Poisson pressure equation, the equation of state is employed to find the pressure

$$p_i = \frac{\rho_0 c_0^2}{\xi} \left[\left(\frac{\rho_i}{\rho_0} \right)^{\xi} - 1 \right], \quad (4)$$

where ρ_0 is a reference density at the initial state and $\xi = 7$ typically for incompressible fluids. c_0 is an artificial sound speed which should be set at least 10 times of the maximum fluid velocity to guarantee fluid density fluctuations below 1%.

The continuity equation is discretized as

$$\begin{aligned} \frac{d\rho_i}{dt} = & \sum_j m_j (\mathbf{v}_i - \mathbf{v}_j) \cdot \nabla_i W \\ & + 2\delta h c_0 \sum_j \frac{m_j}{\rho_j} (\rho_j - \rho_i) \frac{(\mathbf{x}_i - \mathbf{x}_j) \cdot \nabla_i W}{|\mathbf{x}_i - \mathbf{x}_j|^2 + 0.01h^2}, \end{aligned} \quad (5)$$

where the second term of the right-hand side is a diffusive term³⁵ introduced to stabilize the density field during high-frequency oscillations. The parameter δ is set to 0.1 in this study.

In addition, the particle shifting technique is used to evenly distribute SPH particles in the whole domain, especially at the solid–fluid moving interfaces, and to prevent numerical cavity.³⁶

B. SPH-DEM coupling

Following the work of Koshizuka *et al.*,³⁷ the rigid DEM grain *I* is also discretized by a series of SPH particles for SPH-DEM coupling, as shown in Fig. 1. The motion of DEM grains is governed by the Newton’s second law,

$$M_I \frac{d\mathbf{V}_I}{dt} = \sum_{k \in I} m_k \frac{d\mathbf{v}_k}{dt}, \tag{6}$$

$$\mathbf{I}_I \frac{d\boldsymbol{\Omega}_I}{dt} = \sum_{k \in I} m_k (\mathbf{x}_k - \mathbf{X}_I) \times \frac{d\mathbf{v}_k}{dt}, \tag{7}$$

where grain *I* possesses the mass M_I , velocity \mathbf{V}_I , moment of inertia \mathbf{I}_I , angular velocity $\boldsymbol{\Omega}_I$, and center of gravity \mathbf{X}_I . The right-hand side of Eq. (6) is the resultant force on grain *I* summed from the unit forces applied to each discretizing particle (with mass m_k , position \mathbf{x}_k , and velocity \mathbf{v}_k), which mainly include (1) the body force (i.e., gravity), (2) the hydrodynamic force exerted by fluid particles, and (3) the contact force from other DEM grains. Since the rigid grains are discretized by ordinary SPH particles, the hydrodynamic force on a solid particle *k* can be calculated following the same manner in SPH using Eq. (3). The calculation of contact force from other DEM grains is detailed in the following.

The normal contact force is given by a modified, non-linear, Hertzian model,

$$\mathbf{F}_n = k_n \delta_n^{1.5} \mathbf{n} - \gamma_n \delta_n^{0.25} \dot{\delta}_n \mathbf{n}, \tag{8}$$

where k_n is the normal contact stiffness, δ_n is the interparticle overlap, \mathbf{n} is the unit normal vector at the contact, and γ_n is the normal damping ratio. The first exponent 1.5 is derived for contacts between 3D spheres but also roughly applicable for 2D simulations. Hunt and Crossley³⁸ suggested its range of [1, 1.5] for the contact between two parallel aligned cylinders. The stiffness and damping ratio are given by Canelas *et al.*,³⁰

$$k_n = \frac{4}{3} E^* \sqrt{R^*}, \tag{9}$$

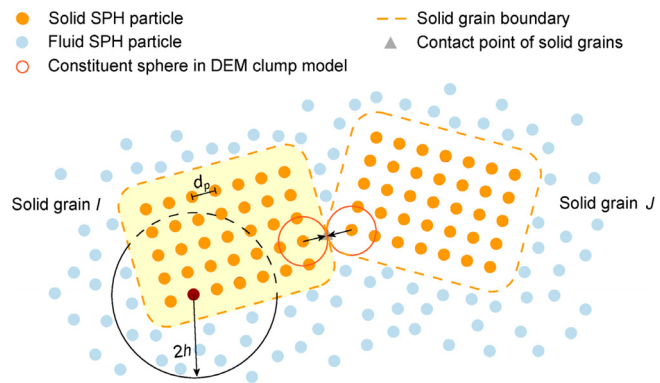


FIG. 1. Illustration of SPH discretization of fluid domain and solid grains.

$$\gamma_n = \frac{2 \ln(e)}{\sqrt{\pi^2 + \ln^2(e)}} \sqrt{k_n M^*}, \tag{10}$$

where e is the coefficient of restitution, and the other parameters are determined as

$$\frac{1}{E^*} = \frac{1 - \nu_I^2}{E_I} + \frac{1 - \nu_J^2}{E_J}, \tag{11}$$

$$R^* = \frac{R_I R_J}{R_I + R_J}, \tag{12}$$

$$M^* = \frac{M_I M_J}{M_I + M_J}, \tag{13}$$

where E_{\blacksquare} , ν_{\blacksquare} , and R_{\blacksquare} ($\blacksquare = I$ or J) are the Young’s modulus, Poisson’s ratio, and radius of the two contacting DEM grains, respectively.

Regarding the tangential contact force, the Coulomb law is modified with a sigmoidal function to render the force continuous with the tangential velocity,^{39,40}

$$\mathbf{F}_t^{\text{trial}} = \mathbf{F}_t^{\text{prev}} + k_t \delta_t \mathbf{t} - \gamma_t \dot{\delta}_t \mathbf{t}, \tag{14}$$

$$|\mathbf{F}_t| = \min\left(\mu |\mathbf{F}_n| \tanh(8\dot{\delta}_t), |\mathbf{F}_t^{\text{trial}}|\right), \tag{15}$$

where $\mathbf{F}_t^{\text{prev}}$ is the previous tangential force, k_t is the tangential contact stiffness, δ_t is the relative tangential displacement, γ_t is the tangential damping ratio, \mathbf{t} is the unit tangential vector, and μ is the friction coefficient. In the study, $k_t = \frac{2}{7} k_n$, $\gamma_t = \frac{2}{7} \gamma_n$.³⁰ It is noted that the contact model also applies to grains with complex shapes, as they are approximately represented by clumped spheres in the study (see Fig. 1). The radius of constituent spheres in the clump model is set to about d_p . The DEM parameters used in all the tests presented in this study are listed in Table I, which are generally applicable for relatively hard grains with negligible deformation.

The symplectic algorithm is applied to carry out time integration. Adaptive time steps³⁰ are calculated according to the Courant–Friedrichs–Lewy (CFL) condition as below

$$\Delta t = C \times \min \left[\min_i \left(\sqrt{\frac{h}{|\mathbf{f}_i|}} \right), \min_i \left(\frac{h}{c_0 + \max_j \frac{(\mathbf{v}_i - \mathbf{v}_j) \cdot (\mathbf{x}_i - \mathbf{x}_j)}{|\mathbf{x}_i - \mathbf{x}_j|^2}} \right), \min \left(\frac{\pi}{50} \sqrt{\frac{k_n}{M^*}} \right) \right], \tag{16}$$

where the CFL coefficient is set to $C = 0.2$ in the study to guarantee numerical stability. The first term on the right-hand side is based on the force per unit mass (\mathbf{f}_i) applied on the SPH particle *i*, the second term combines the CFL condition and the viscous time step control, and the third term is the constraint of DEM stability. The SPH-DEM

TABLE I. DEM parameters in the coupled SPH-DEM simulations.

Young’s modulus E (Pa)	Poisson’s ratio ν	Friction coefficient μ	Coefficient of restitution e
10^8	0.2	0.45	0.6

coupling algorithm is illustrated in Fig. 2. The main calculation steps are parallelized and executed on GPU, which is a welcome feature available in DualSPHysics.

III. VALIDATION

To validate the fully resolved SPH-DEM model for fluid-grain mixture flows, five benchmark tests including water entry of a disk, sedimentation of an ellipse in a vertical channel, periodic flow around a sunflower-shaped object, pair-disk trajectories in a shear flow, and settlement of two vertically aligned disks have been conducted and compared with the available experimental and numerical results from the literature. All the simulations in the study are performed in 2D.

A. Water entry of a disk

The water entry problem of a disk is simulated with the SPH-DEM method. The problem was experimentally investigated by Greenhow and Lin⁴¹ and later modeled using the constrained interpolation profile (CIP) method by Zhu *et al.*⁴² The disk has a diameter $D = 0.125$ m and is dropped at a height of 0.5 m above the water surface, as shown in Fig. 3. The water depth is 0.3 m. The solid-to-fluid density ratio is either 0.5 or 1, corresponding to the half-buoyant or neutrally buoyant case, respectively. Sensitivity analysis on discretization is performed considering different initial SPH particle spacing d_p (i.e., $d_p/D = 1/20, 1/25,$ and $1/40,$ respectively).

Figure 4 gives the evolution of water-entry depth in both half-buoyant and neutrally buoyant cases, comparing the present SPH-

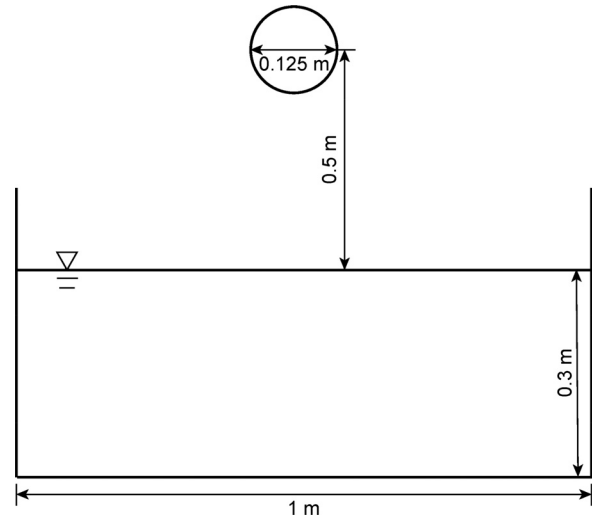


FIG. 3. Numerical model of the water-entry problem.

DEM results with those from the experimental⁴¹ and CIP⁴² studies. The SPH-DEM results converge to the CIP simulation and experimental results with the refinement of discretization. Specifically, when d_p/D is no greater than $1/25$, the SPH-DEM and CIP methods have comparable performances and both correctly capture the evolution of water-entry depth in the two buoyant cases. Therefore, the initial SPH particle spacing is set to be $d_p/D \leq 1/25$ in the following tests. It is also observed that the disk de-acceleration is slower when its density is larger. At the entry depth of 0.3 m, the neutrally buoyant disk rebounds after it comes into contact with the container bottom.

B. Sedimentation of an ellipse in a vertical channel

A tilted ellipse falling under gravity in a closed vertical channel fully filled with fluid is considered. The problem configuration is

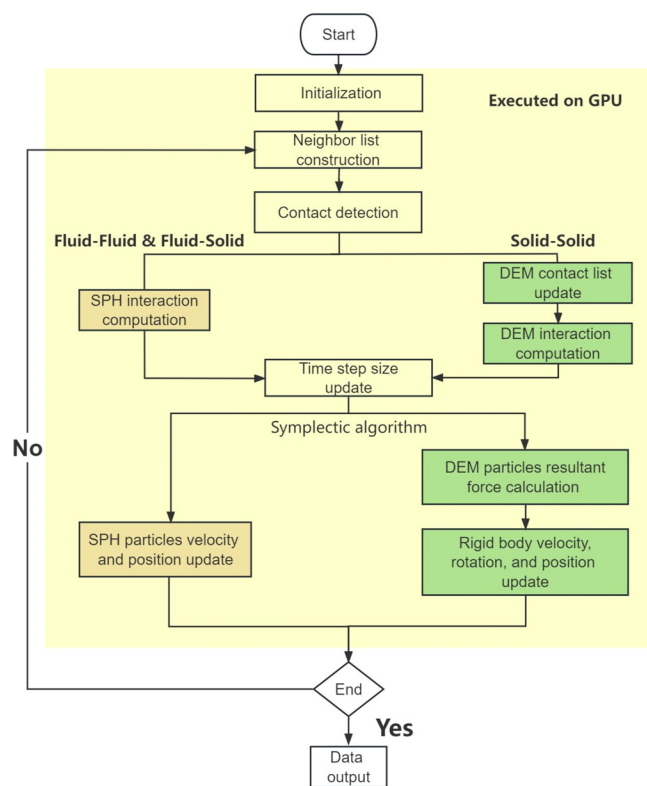


FIG. 2. The flow chart of SPH-DEM coupling algorithm.

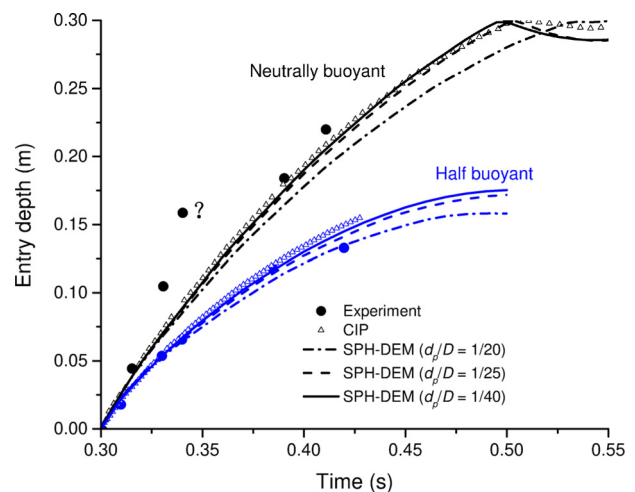


FIG. 4. Evolution of water entry depth from the experimental,⁴¹ CIP,⁴² and present SPH-DEM studies (the question mark put by Greenhow and Lin⁴¹ indicates that this data point is unreasonable).

23 August 2023 04:08:55

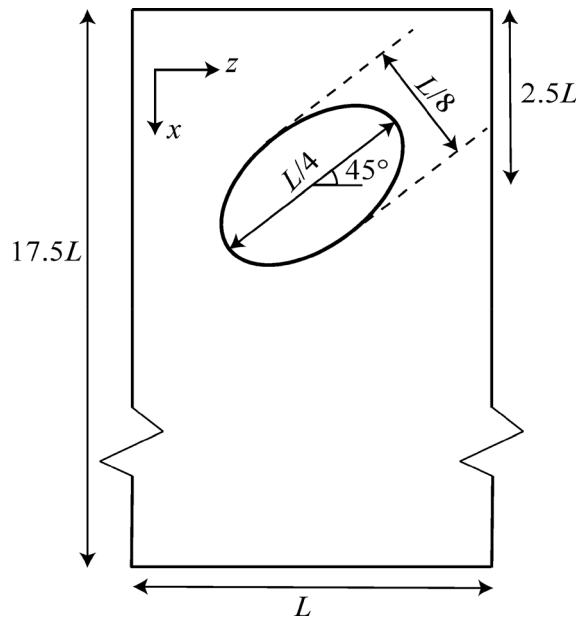


FIG. 5. Depiction of an ellipse falling in a vertical channel closed by four walls on all the boundaries (not to scale).

shown in Fig. 5. The domain width and height are L (0.004 m) and $17.5L$, respectively. The ellipse has an aspect ratio $AR = 0.5$ and its major diameter is $L/4$ (i.e., the blockage ratio is 4). Its center is initially $2.5L$ below the top surface with an inclination angle of 45° . The solid-to-fluid density ratio is 1.5. The initial SPH particle spacing is $d_p = L/104$.

Figure 6 plots the horizontal position and orientation of the ellipse vs the vertical position, respectively. Reasonable agreements are observed in comparison with the LBM results of Xia *et al.*,⁴³ IB-LBM results of Suzuki and Inamuro,⁴⁴ and incompressible SPH (ISPH) results of Khorasanizade and Sousa.⁴⁵

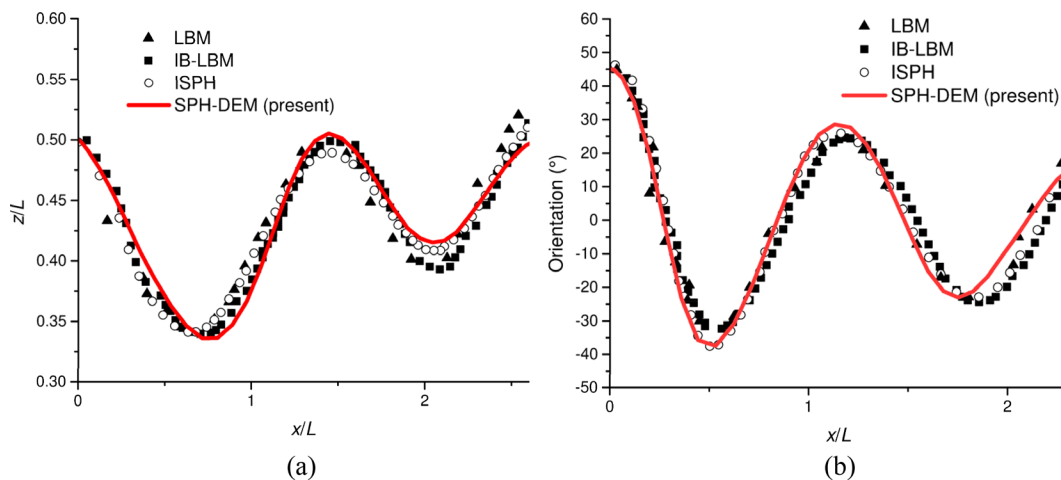


FIG. 6. Ellipse (a) horizontal position and (b) orientation vs its vertical position (LBM,⁴³ IB-LBM,⁴⁴ and ISPH⁴⁵).

C. Periodic flow around a sunflower-shaped object

Aiming to demonstrate the SPH-DEM capability in coping with complex geometries with sharp concave corners, the flow around a 13-petal sunflower-shaped object is analyzed. This test was described in Pan *et al.*,⁴⁶ consisting of periodic flow through a plane channel with dimension $0.1 \times 0.1 \text{ m}^2$ and a sunflower-shaped body fixed at the center. Flow is driven by a body force of $1.5 \times 10^{-8} \text{ m/s}^2$ imposed in the longitudinal x -direction. The initial SPH particle spacing is set to $d_p = 0.0005 \text{ m}$, same as in Pan *et al.*⁴⁶

A steady flow solution is obtained for the specified conditions. The contour of longitudinal velocity is portrayed in Fig. 7, along with the result from Pan *et al.*⁴⁶ A good agreement is found between the two studies from the comparison. More detailed assessment is performed in Fig. 8, where the longitudinal velocity profiles along the transverse y -direction are displayed at two distinct locations: across the center of the object (i.e., $x = 0.05 \text{ m}$) and at the outlet boundary (i.e., $x = 0.1 \text{ m}$). The present results agree well with both the SPH and finite element method (FEM) predictions reported by Pan *et al.*⁴⁶

D. Pair-disk trajectories in a shear flow

In this subsection, the pair-disk trajectories in a Newtonian fluid are studied. This case is relevant to suspension flows where hydrodynamic interactions are of primary importance. The problem is schematically shown in Fig. 9 with the same geometric parameters as in Choi *et al.*,⁴⁷ i.e., the domain length $L = 4$ and width $H = 1$ (in the simulation, 1 length unit corresponds to a physical length of 0.12 m). Two equally sized ($R = 0.1$) smooth disks are freely suspended in a linear shear flow, and their initial positions are $(-L_x, L_y)$ and $(L_x, -L_y)$ with $L_x = 0.5$ fixed in the study. The top and bottom walls move at opposite constant velocities to generate a laminar Newtonian flow with periodic boundary condition applied in the shear direction. The Reynolds number is measured to be about $Re_p = 0.0288$ [see Eq. (17)] so that the inertia effect is regarded as negligible. The original SPH particle spacing is $d_p = L/600$.

Trajectories for varying initial vertical positions of the two disks ($\pm L_y$) are depicted in Fig. 10, compared with the available FEM

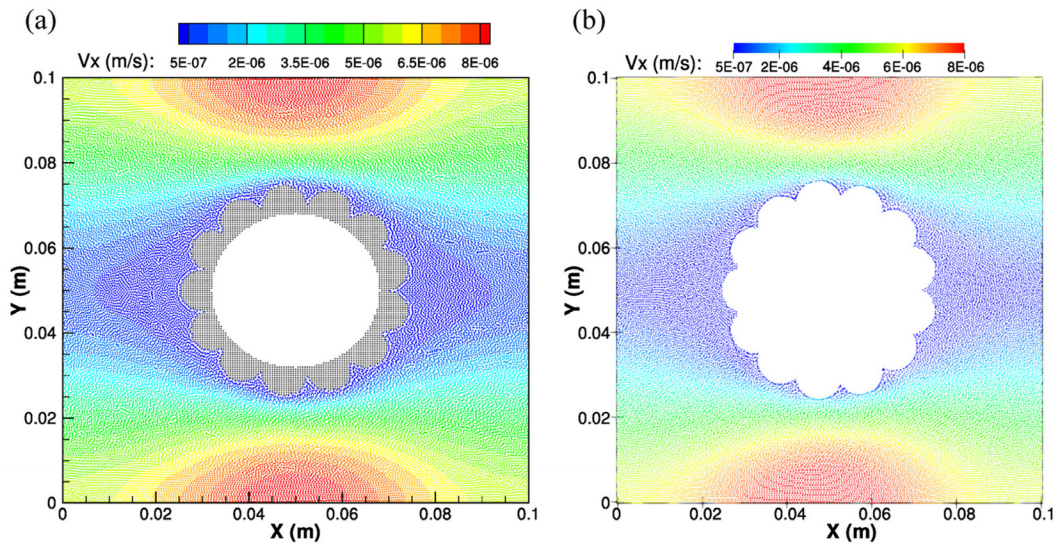


FIG. 7. Contours of the longitudinal velocity at the steady state from (a) [Reproduced with permission from Pan *et al.*, J. Comput. Phys. 259, 242 (2014), Copyright 2014 Elsevier.]⁴⁶ and (b) present SPH-DEM study.

solutions.⁴⁷ It shows that the two disks repel each other and their trajectories are reversed like U-turns when their initial separations are small (e.g., $L_y = 0.02, 0.04,$ and 0.06). However, the two disks keep going in their sheared directions and pass each other when their initial separations become larger (e.g., $L_y = 0.08$ and 0.10). The comparisons exhibit good match between the present SPH-DEM and existing FEM predictions, implying that the hydrodynamic forces are accurately computed when the particles get close. The minor difference between the two studies may be attributable to the small inertia effect (Re_p slightly larger than 0) and particle artificial roughness resulting from discretization in this study.

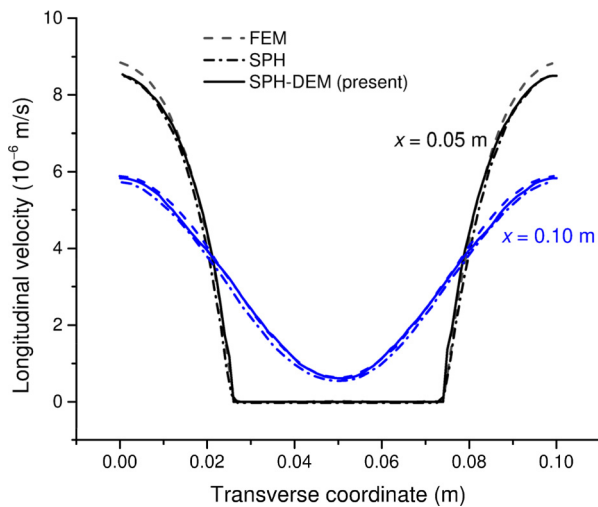


FIG. 8. Longitudinal velocity profiles along the transverse direction (FEM and SPH results from Pan *et al.*)⁴⁶.

E. Settlement of two vertically aligned disks

To further demonstrate the predictive capability of the proposed SPH-DEM for inter-grain collision problems, the settlement of two disks in a closed container filled with Newtonian fluid is investigated. The two disks have identical density and radius and are originally vertically aligned with some offset and released from rest. The model parameters are summarized as follows: the domain length 2 cm and height 6 cm, disk radius 0.125 cm and initial center positions (1 cm, 4.5 cm) and (1 cm, 5 cm), solid-to-fluid density ratio 1.5, fluid kinematic viscosity 10^{-6} m²/s, and initial SPH particle spacing $d_p = 0.00625$ cm.

The drafting-kissing-tumbling (DKT) phenomenon is clearly displayed in Fig. 11 at different time instants. First, the trailing disk catches up with the leading one due to reduced drag in the wake of the leading disk ($t = 0.15$ s). Next, the two disks are close enough to be almost touching, corresponding to the kissing stage ($t = 0.2$ s). Nevertheless, the contact is unstable and will be broken easily, leading to the tumbling of the two disks ($t = 0.3$ s).

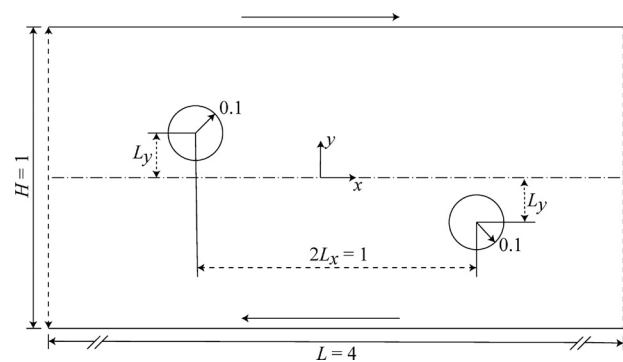


FIG. 9. Geometry for pair-disk trajectories in a simple shear flow.

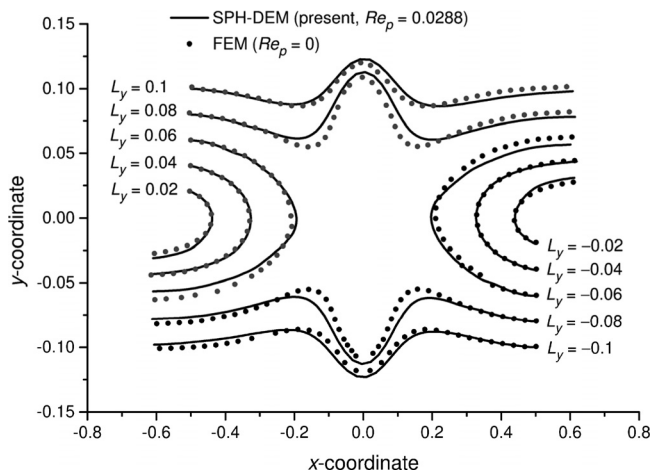


FIG. 10. Pair-disk trajectories in a shear flow from SPH-DEM and FEM.⁴⁷

Figure 12 presents the evolution of vertical position and velocity of the two disks, comparing with the FDM results of Glowinski *et al.*¹⁷ and IBM results of Uhlmann.⁴⁸ The present results are generally in good agreement with existing ones, except for some deviations in the tumbling separation stage as expected. The difference mainly arises from the distinct grain collision strategies adopted in these numerical methods. Glowinski *et al.*¹⁷ and Uhlmann⁴⁸ simply considered a short-range repulsive force in the normal direction to prevent inter-grain penetration, whereas the contact model adopted in this study is more accurate in describing the collision behavior considering contact forces in both normal and tangential directions.

IV. SUSPENSION FLOW

In this section, suspensions of monodisperse solid disks of radius R confined between two parallel no-slip walls are simulated to analyze

their viscometric behavior under constant shear rate. Gravity is ignored in the simulation. The computational domain has a size L in the flow direction (x) and a width H in the gradient direction (z). The size relations are $L = 2H = 100R$. The x -directed shear flow is generated by moving the top wall with a speed of U_w so that the equivalent shear rate is $\dot{\gamma} = U_w/H$. The periodic boundary condition is applied in the x direction. The 2D solid fraction is denoted by ϕ . In addition, two dimensionless numbers are used to describe the inertia effect of suspensions. The particle Reynolds number is defined as the ratio of the fluid inertial stress to the fluid viscous stress,

$$Re_p = \frac{4R^2\dot{\gamma}\rho_f}{\mu_f}, \tag{17}$$

where ρ_f and μ_f are the fluid density and dynamic viscosity, respectively. Another important parameter characterizing the suspension behavior is the Bagnold number, defined as the ratio of the grain inertial stress due to collision to the fluid viscous stress,^{49,50}

$$Ba = \frac{\phi}{1-\phi} \frac{4R^2\dot{\gamma}\rho_s}{\mu_f} = \frac{\phi}{1-\phi} \frac{\rho_s}{\rho_f} Re_p, \tag{18}$$

where ρ_s is the solid grain density. It is seen from Eq. (18) that the solid fraction, density ratio, and particle Reynolds number all contribute to the suspension flow properties. Hence, their effects will be examined separately in the following.

By varying the grain number (i.e., solid fraction), density ratio, and shear rate, different particle Reynolds and Bagnold numbers can be realized, resulting in different inertia effects of suspension flows. To further consider the influence of grain shape, suspensions of elliptic and sunflower-shaped grains are simulated for comparison, where two shape descriptors, i.e., aspect ratio and convexity, are used for quantitative analysis. These grains have the same area as the circular ones with an equivalent radius equal to R . The grain convexity (CV) is

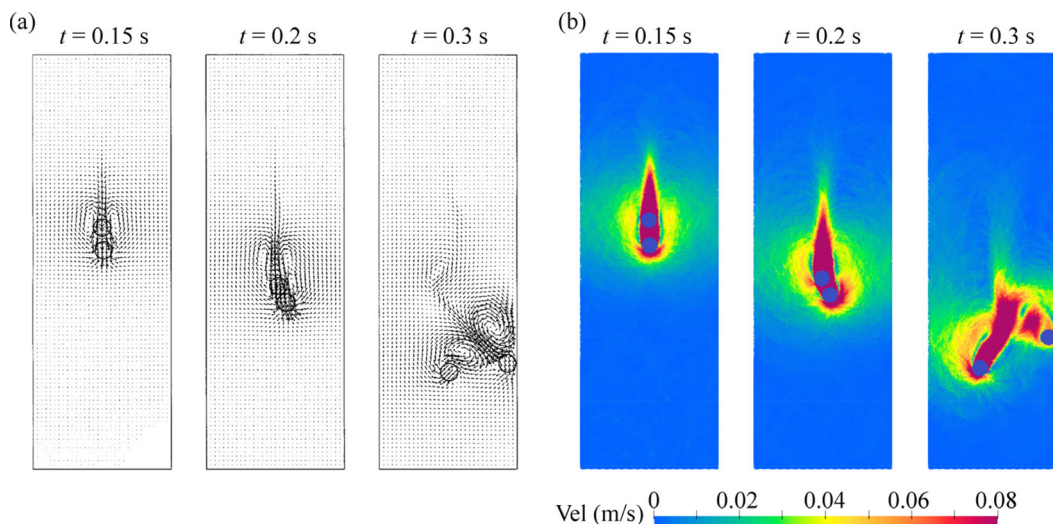


FIG. 11. Drafting–kissing–tumbling phenomenon at different time steps using the (a) FDM¹⁷ [Reproduced with permission from Glowinski *et al.*, J. Comput. Phys. 169, 363 – 426 (2001). Copyright 2001 Elsevier.] and (b) present SPH-DEM method.

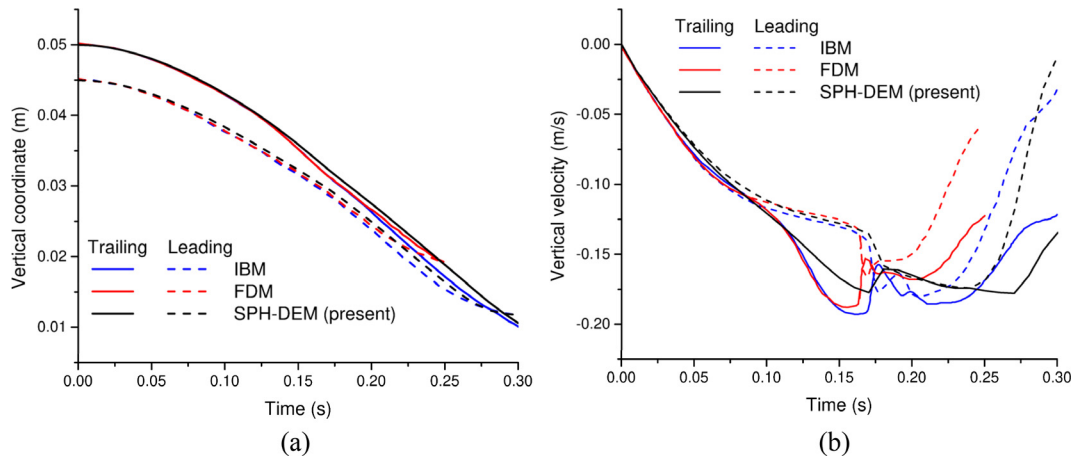


FIG. 12. Comparison of vertical (a) positions and (b) velocities of the two falling disks.

defined as its area divided by the area after filling all the concavities in its perimeter.⁵¹

The model parameters of different test cases are summarized in Table II. Results are collected and analyzed after the mixture flow reaches a statistically steady state, as shown in Fig. 13. The shear stress τ is directly obtained from the shear force acting on the boundary walls, and the effective viscosity of the suspension is calculated from

$$\mu_s = \frac{\tau}{\dot{\gamma}}. \tag{19}$$

Sensitivity analysis on the effect of SPH particle discretization is conducted for a typical high-concentration ($\phi = 47\%$ and $Re_p = 0.15$) suspension of circular grains, considering $d_p/D = 1/15, 1/20, 1/25, 1/30,$ and $1/35,$ respectively. The evolution of relative viscosity

$\mu_r,$ defined as the ratio of effective viscosity of the suspension to that of the fluid, i.e., $\mu_r = \mu_s/\mu_f,$ is shown in Fig. 14, which suggests apparent convergence of the results as d_p decreases. In particular, when d_p/D decreases from $1/30$ to $1/35,$ the deviation of results is smaller than 5%. Therefore, d_p is set to $D/30$ in the tests of this section, which strikes a good compromise between numerical efficiency and accuracy.

A. Relative viscosity

Figure 15 illustrates the relative viscosity flow curves for suspensions of circular grains with different ranges of solid concentration and density ratio. The shear-thickening phenomenon is observed in all cases as μ_r increases steadily with $\dot{\gamma},$ especially for large solid

TABLE II. Parameters for suspension flows.

Solid concentration: ϕ	Particle Reynolds number: Re_p	Density ratio: ρ_s/ρ_f	Bagnold number: B_a	Remark
14%	0.15	2.65	0.06	Bold-font cases include tests on suspensions of elliptic (AR = 0.33, 0.66) or sunflower-shaped (CV = 0.91, 0.84, 0.74) grains.
	0.30		0.13	
25%	0.45	2.65, 10	0.19, 0.73	
	0.15	2.65, 10	0.13, 0.48	
	0.30		0.25, 0.96	
36%	0.45	2.65, 10	0.38, 1.44	
	0.15	2.65, 10	0.21, 0.81	
	0.225	2.65	0.32	
	0.30	2.65, 10	0.43, 1.62	
	0.375	2.65	0.54	
47%	0.45	2.65, 10	0.64, 2.43	
	4.5	2.65	6.44	
	0.15	2.65	0.34	
	0.225		0.51	
	0.30		0.68	
	0.375		0.85	
	0.45		1.03	

23 August 2023 04:08:55

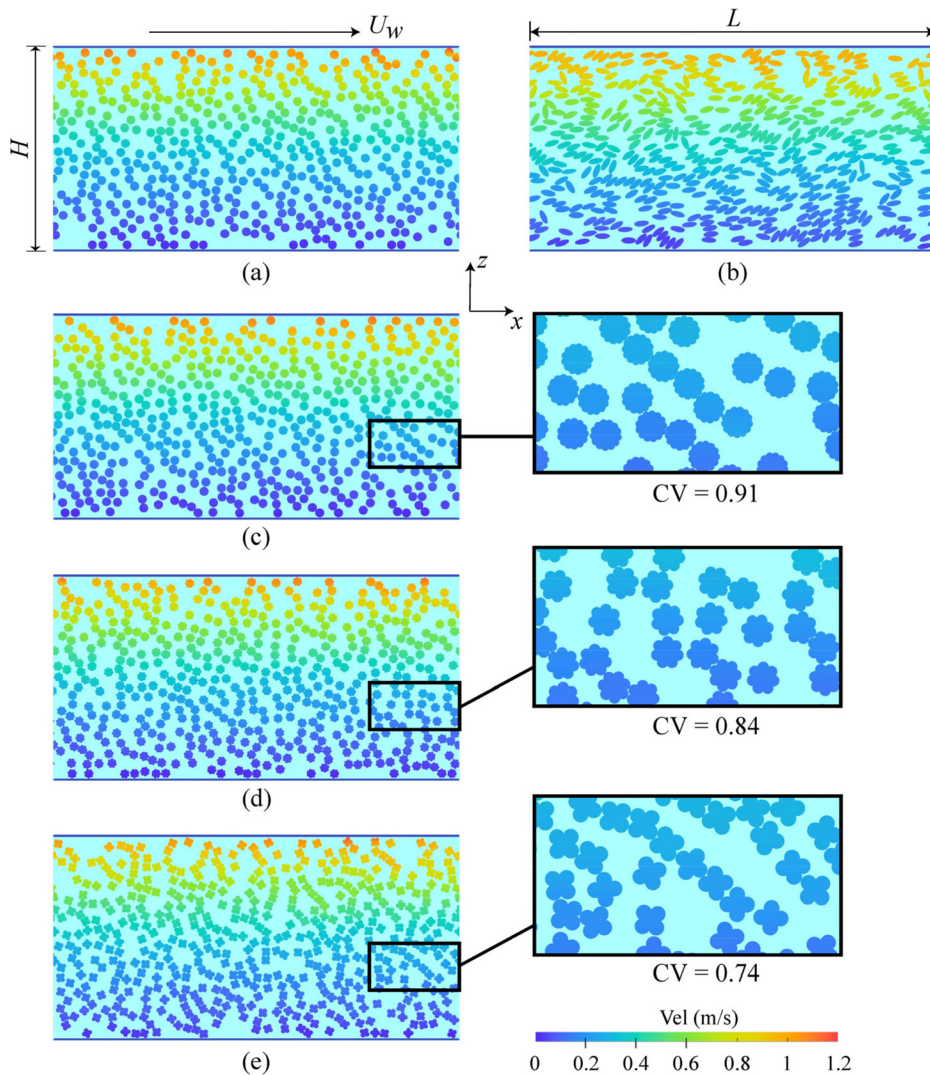


FIG. 13. Steady-state suspension flows ($\phi = 36\%$, $Re_p = 4.5$) mixed with (a) disks, (b) ellipses (AR = 0.33), and (c)–(e) sunflower-shaped grains (CV = 0.91, 0.84, and 0.74, respectively).

concentrations (e.g., $\phi \geq 36\%$) when the upsurge of viscosity with $\dot{\gamma}$ becomes noteworthy. The non-Newtonian behavior becomes more distinct with larger ϕ and density ratio. With ρ_s/ρ_f increasing from 2.65 to 10, the viscosity flow curves for the two solid fraction cases $\phi = 25\%$ and 36% shift upward. Zhou and Prosperetti²² reported similar observations for suspensions of noncolloidal particles albeit with larger Reynolds numbers in their study.

The dependence of μ_r on solid concentration ϕ for suspensions of both circular and non-circular grains with $\rho_s/\rho_f = 2.65$ is shown in Fig. 16. Results are presented together with the experimental data of Zarch *et al.*⁵² for soil–water mixture with $\rho_s/\rho_f = 2.62$ and $10^{-3} < Re_p < 10$, Mueller *et al.*⁵³ for mixture of silicone oil and glass beads with $\rho_s/\rho_f = 2.74$ and $Re_p < 10^{-6}$, and numerical data of Gallier *et al.*¹⁶ with neutrally buoyant Stokes suspensions of spheres. The volume fraction in 3D suspensions is transformed to the area fraction by multiplying 3/2 according to previous studies for comparison between 2D and 3D results.⁵⁴ It is evident from Fig. 16 that μ_r

increases at a greater rate with larger Re_p which partly explains the more rapid increasing $\mu_r - \phi$ curve in Zarch *et al.*⁵² compared to the results of Gallier *et al.*¹⁶ and Mueller *et al.*⁵³ The curve of $Re_p = 0.3$ in the present study fits well with the data of soil–water mixture in Zarch *et al.*⁵² In addition to the role of inertia, the grain shape also has a significant impact on the non-Newtonian flow property. At the same Re_p and ϕ , a prominent increase in μ_r is found with decreasing AR and CV. The effects of inertia and grain shape will be further explored in Secs. IV B–IV E.

B. Stress contributions

The different roles of inertia and grain shape on suspension viscosity can be better understood by studying their contributions to the overall shear stress. We implemented the procedure developed by Batchelor⁵⁵ to calculate the bulk stress generated by a flowing suspension in terms of area averages. The relative viscosity can be written as²¹

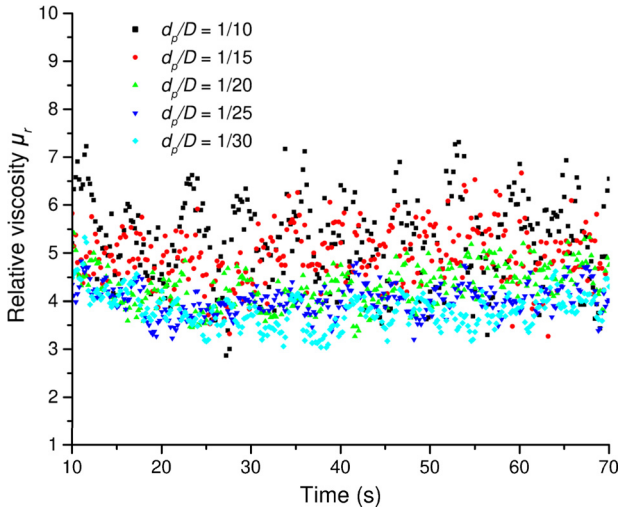


FIG. 14. Sensitivity analysis on discretization for a sheared suspension of circular grains.

$$\mu_r = 1 + \Sigma_{xz}^g, \quad (20)$$

where Σ_{xz}^g represents the grain-induced stress defined as follows:

$$\Sigma_{xz}^g = \frac{1}{\mu_f \dot{\gamma}} \left(s_{xz} + \hat{\sigma}_{xz}^c \right) - \underbrace{(1 - \phi) B_a \langle \tilde{u}_x^g \tilde{u}_z^g \rangle - (1 - \phi) Re_p \langle \tilde{u}_x^f \tilde{u}_z^f \rangle}_{\text{Reynolds stress}}, \quad (21)$$

where $\langle \blacksquare \rangle$ denotes the ensemble averaged quantity. The first term on the right-hand side denotes the hydrodynamic and collisional stresslets defined by

$$s_{xz} = \frac{1}{2LH} \sum \left(r_z f_x^h + r_x f_z^h \right), \quad (22)$$

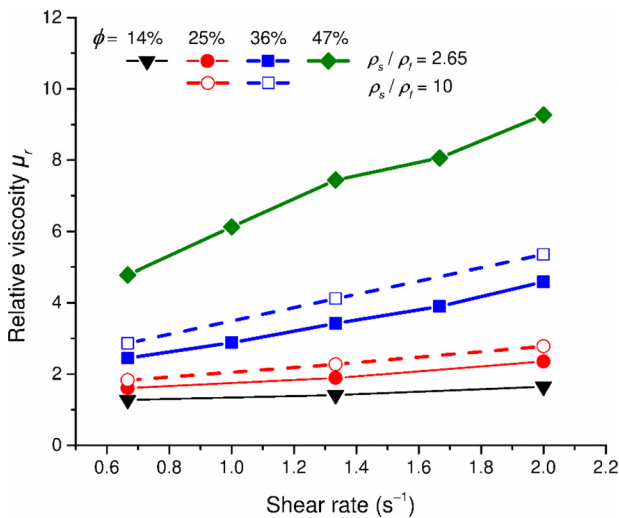


FIG. 15. Viscosity flow curves for different ranges of solid concentration and density ratio for suspensions of circular grains.

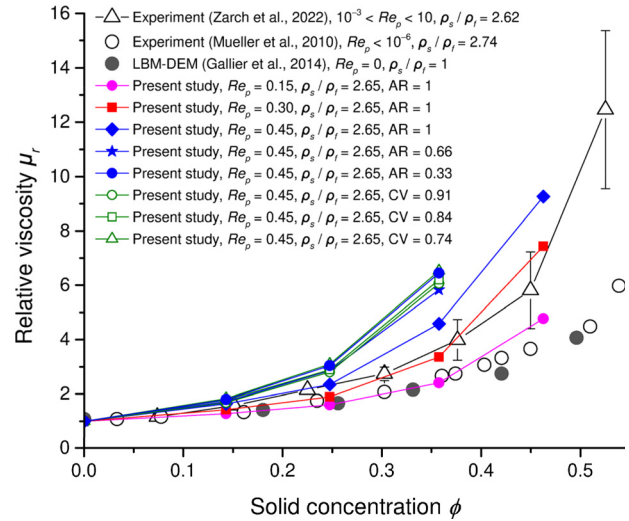


FIG. 16. Relationship between relative viscosity and solid concentration.

$$\hat{\sigma}_{xz}^c = \frac{1}{2LH} \sum \left(r_z f_x^c + r_x f_z^c \right), \quad (23)$$

where f_x^h and f_x^c ($\blacksquare = x$ or z) are the hydrodynamic force and inter-grain collisional force exerted on the grain, respectively; r_{\blacksquare} is the branch vector connecting the grain centroid and the point of force application. The summation is carried out over all the grains. The last two terms represent the Reynolds stress from fluctuations of grains and fluid particles. The acceleration stress is ignored in the study due to its insignificant contribution. The velocity fluctuations of grain and fluid ($\tilde{u}_{\blacksquare}^g$ and $\tilde{u}_{\blacksquare}^f$) are calculated as $\tilde{u}_{\blacksquare}^g = u_{\blacksquare}^g - \bar{u}_{\blacksquare}$ and $\tilde{u}_{\blacksquare}^f = u_{\blacksquare}^f - \bar{u}_{\blacksquare}$, where \bar{u}_{\blacksquare} is the undisturbed velocity for a uniformly sheared fluid.⁵⁶ The Reynolds stress cannot be ignored when the bulk Reynolds number is out of the range of laminar flows.⁵⁷

The relative viscosity obtained from both the shear stress on the walls [i.e., Eq. (19)] and the bulk stress calculated using Eq. (20) for different cases is displayed in Fig. 17. The two measures show an overall reasonable agreement although there is a deviation of about 7% for the AR = 0.66 case which owes to the increased boundary effect as to be shown in Fig. 23(a), consistent with the findings in Kulkarni and Morris.²¹

The contributions of each term (i.e., fluid viscous stress, grain hydrodynamic stress s_{xz} , collision stress $\hat{\sigma}_{xz}^c$, and Reynolds stress) to the overall viscosity are evaluated for various Re_p and ϕ in Fig. 18. Irrespective of Re_p , the contributions from both grain hydrodynamics and collision increase, resulting in an increase of total relative viscosity. The grain-related stress ($s_{xz} + \hat{\sigma}_{xz}^c$) is dominant to the total stress when $\phi \geq 36\%$. More specifically, for $14\% \leq \phi \leq 36\%$, the contribution of particle–fluid interaction (s_{xz}) plays a leading role in the enhancement of overall viscosity. However, the collision ($\hat{\sigma}_{xz}^c$) contribution to viscosity significantly rises when ϕ increases from 36% to 47% and eventually occupies 39.5% of the overall viscosity in the case $Re_p = 0.45$. The inter-grain collision, therefore, accounts for the exponential growth of μ_r presented in Fig. 16.

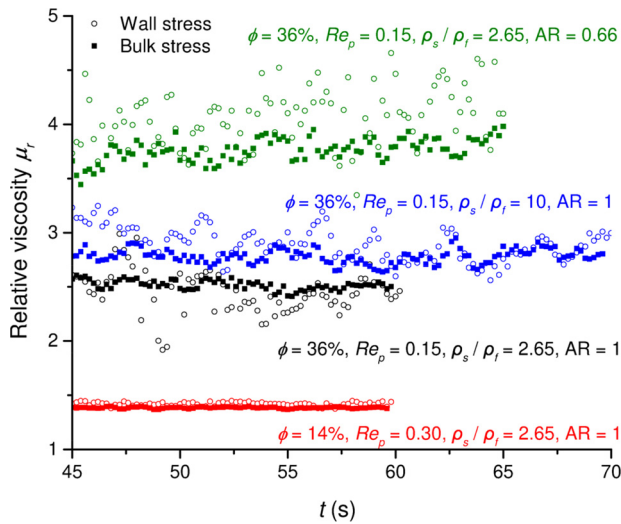


FIG. 17. The instantaneous relative viscosity of a sheared suspension measured from the wall and the bulk.

By comparing the results of different Re_p in Fig. 18, it is found that increasing Re_p leads to the rising of both hydrodynamic and collision stresses. The inter-grain collision contribution increases dramatically with the growth of Re_p , especially for $\phi \geq 36\%$, which may explain the more significant shear-thickening phenomenon for $\phi \geq 36\%$ in Fig. 15.

Figure 19 indicates that the grain-related contribution (Σ_{xz}^g) to viscosity is affected by grain density for both $\phi = 25\%$ and 36% cases. As grain density becomes larger, both collision and grain hydrodynamics show a gradual rise while Reynolds stress caused by disturbance of grains enhances greatly, especially at large Re_p . It well explains the observation in Fig. 15. In spite of the surge of velocity fluctuations caused by grain inertia, the contribution of Reynolds stress to

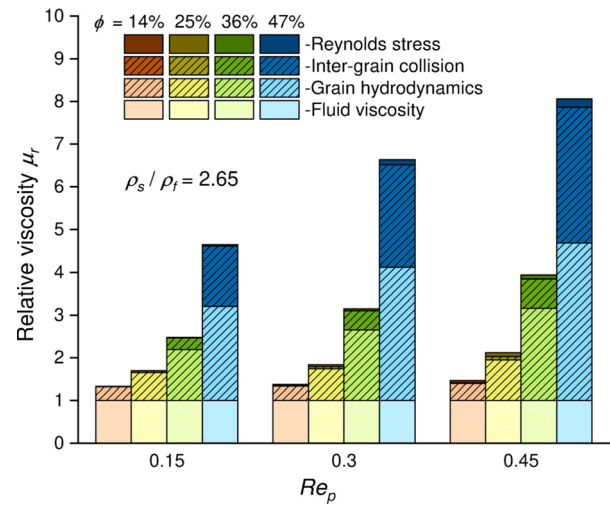


FIG. 18. Contributions of Reynolds stress, inter-grain collision, grain hydrodynamics, and fluid viscosity to the overall viscosity for suspensions of circular grains.

the total stress is generally below 15% and the flow is still in the inertial shear-thickening regime, far from the turbulent-like regime.

The rheology of suspensions with elliptic and sunflower-shaped grains is investigated to explore the influence of grain shape. Figure 20(a) shows that as AR decreasing, the grain-related stresslet ($s_{xz} + \hat{\sigma}_{xz}^c$) grows which results in the steady increase of total relative viscosity, whereas AR has less significant effect on Reynolds stress. Moreover, the effect of AR on inter-grain collision intensifies for larger Re_p . Conversely, the contribution from grain hydrodynamics increases when AR decreases from 1 to 0.66 and remains roughly constant with further decreasing of AR. The role of CV to the relative viscosity of suspension is displayed in Fig. 20(b). A growth of particle-related contribution is found as CV decreases. Such increases are more notable when CV drops from 1 to 0.91 and from 0.84 to 0.74, compared with

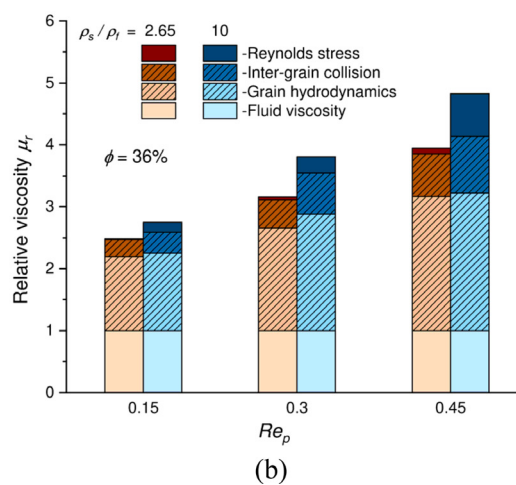
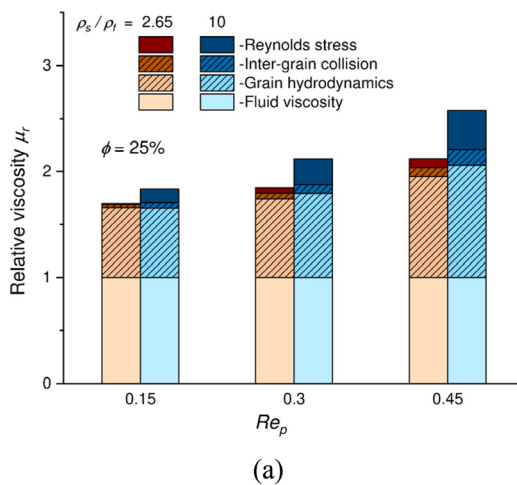


FIG. 19. Contributions of Reynolds stress, inter-grain collision, grain hydrodynamics, and fluid viscosity to overall viscosity with different solid concentrations for suspensions of circular grains: (a) $\phi = 25\%$ and (b) $\phi = 36\%$.

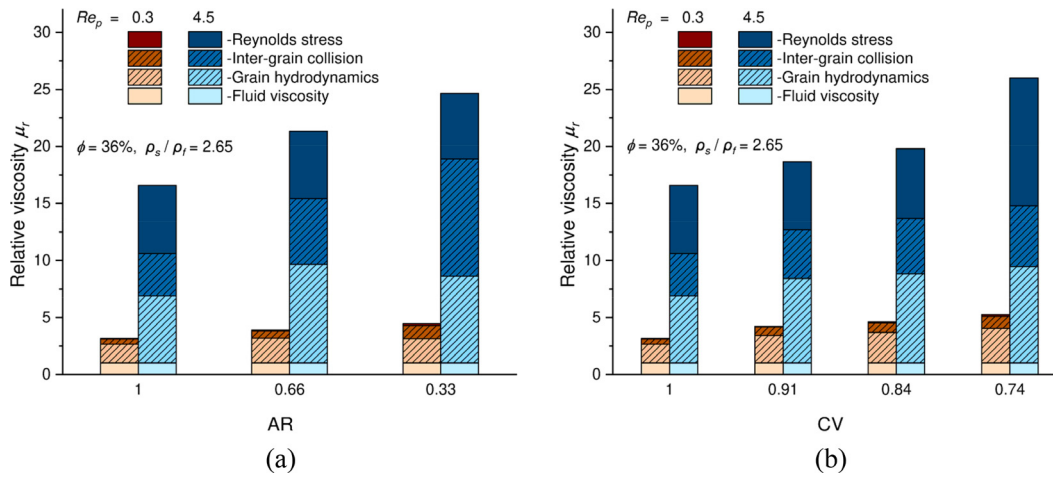


FIG. 20. Contributions of Reynolds stress, inter-grain collision, grain hydrodynamics, and fluid viscosity to overall viscosity with different grain shapes: (a) aspect ratio and (b) convexity.

that when CV varies in the range between 0.91 and 0.84, which exhibits a similar trend as average grain rotation to be shown in Fig. 28(b). More specifically, the marked growth from CV = 1 to 0.91 is mainly due to the increase of fluid–grain interactions (s_{xz}) for both Re_p . As CV decreases from 0.84 to 0.74, the surging velocity fluctuations resulting from grain concavity play a significant role in the increase of bulk viscosity.

C. Profiles of solid concentration and velocity

The solid concentration profile is first presented to characterize the grain layering and the near-wall effects on suspension flows, as it is a possible cause to shear-thickening of suspensions. This is achieved by dividing the computational domain into 250 equally sized layers parallel to the walls and calculating the time-averaged solid area fraction in each layer during the steady state.

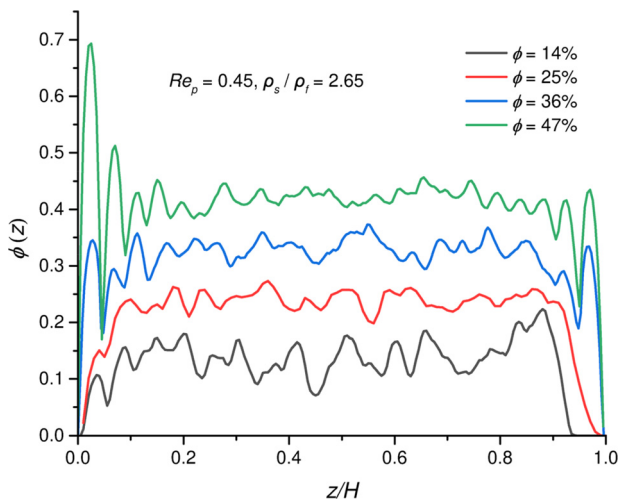


FIG. 21. Time-averaged solid area fraction across the domain width with varying bulk concentrations for suspensions of circular grains.

A local concentration peak near the stationary wall ($z/H = 0$) is clearly visible with $\phi = 47\%$ for the case $Re_p = 0.45$ and $\rho_s/\rho_f = 2.65$ shown in Fig. 21, though not as pronounced as in 3D systems reported elsewhere.¹¹ The formation of stable solid layers near the wall may be resulted from the strong grain–wall interaction. The local concentrations grow to the bulk concentration values faster and peaks closer to the wall as ϕ increases, in agreement with the results of Kromkamp *et al.*,¹¹ Picano *et al.*,⁵⁸ and Yeo and Maxey.⁵⁹

Figure 22 presents the flow profiles for $\phi = 36\%$ with different Re_p and ρ_s/ρ_f , indicating that the local solid fraction tends to rise slightly faster and higher with increasing Re_p and grain density. Nevertheless, Re_p and grain density play an insignificant role in the distribution of local solid fraction in the bulk region away from the boundary walls, which is consistent with the finding in Zhou and Prosperetti.²²

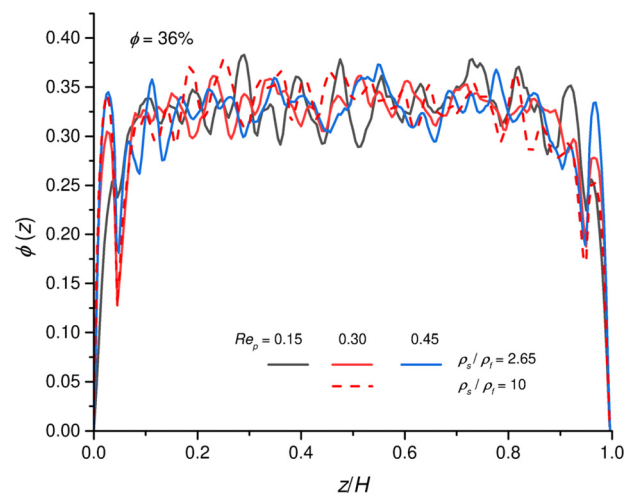


FIG. 22. Time-averaged solid area fraction across the domain width with varying Re_p and ρ_s/ρ_f for suspensions of circular grains.

23 August 2023 04:08:55

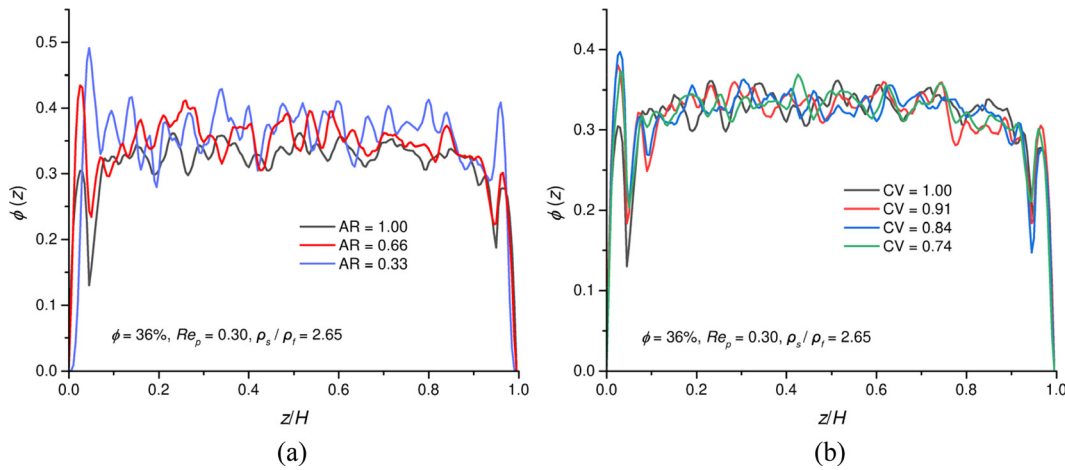


FIG. 23. Time-averaged solid area fraction across the domain width with varying (a) aspect ratio and (b) convexity.

In addition, to show the influence of grain shapes, the flow profiles for $\phi = 36\%$, $Re_p = 0.30$, and $\rho_s/\rho_f = 2.65$ with varying AR and CV are displayed in Fig. 23. The local concentration near the stationary wall increases as both AR and CV deviate from unity. However, the three cases with CV in the range between 0.91 and 0.74 show similar near-wall peak concentration values.

Additionally, the velocity profiles of fluid (nearly identical for solid grains) for different solid concentration, inertia, and shape of grains are shown in Fig. 24 to further explore the influence of wall effect. Near the two walls ($0 \lesssim z/H \lesssim 0.04$ and $0.96 \lesssim z/H \lesssim 1$), the slopes of the curves are steeper than the 1:1 reference line. The enhancement of velocity gradient is more pronounced in higher solid concentration and smaller aspect ratio and convexity cases, where strong layering of grains near the walls is also observed. It seems that the presence of grains near the wall may create a region of increasing velocity gradient, known as the slip layer. The smaller velocity gradient in the bulk of the system (i.e., away from the walls) explains the lower bulk stress than the wall stress presented in Fig. 17.

D. Pair microstructure

The pair microstructure is characterized by the pair distribution function $g(r, \theta)$ defined as the probability of finding a grain at the distance r and polar angle θ to a given grain. Particularly, the probability of the nearest neighbors, i.e., $2R < r < 2.1R$, is examined in the study.

As previously shown in Fig. 10, the pair-particle trajectories are fore-aft symmetric in the dilute pure hydrodynamic limit ($Re_p \approx 0$) owing to the reversibility of Stokes equations.⁴⁷ However, the symmetry can be broken by the Brownian motion,⁵ inter-grain contacts,^{16,58} and finite inertia.²¹ In this study, the effects of the latter two factors are analyzed as presented in Figs. 25 and 26 with varying Re_p , ϕ , ρ_s , and CV. Considering the radial symmetry, only results in the range $0 \leq \theta < 180^\circ$ are shown.

As shown in Fig. 25, the pair distribution functions exhibit a clear asymmetric pattern with elevated probability density in the compressional quadrant ($\theta > 90^\circ$) and a marked depletion zone around the extension axis. When ϕ increases, there are accumulating probabilities

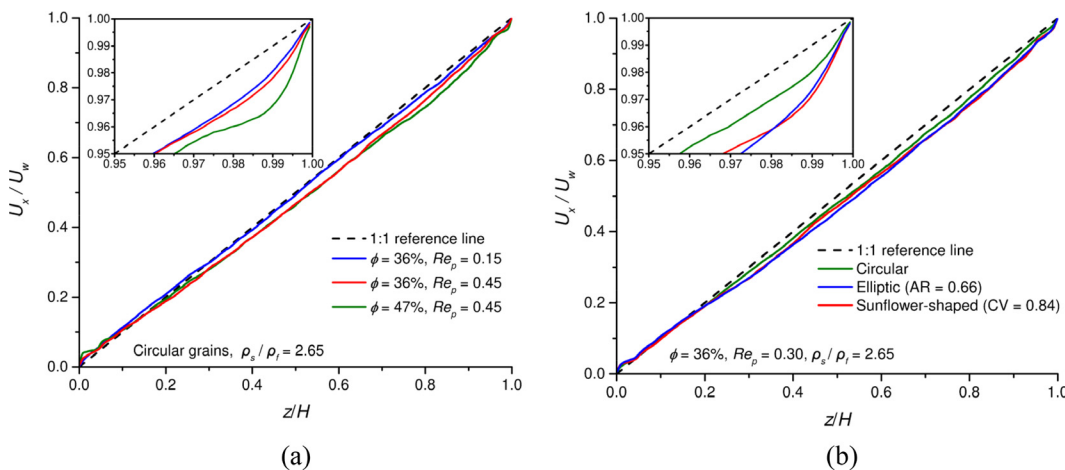


FIG. 24. Time-averaged velocity profiles across the domain width with varying (a) solid concentration and Re_p and (b) grain shape.

23 August 2023 04:08:55

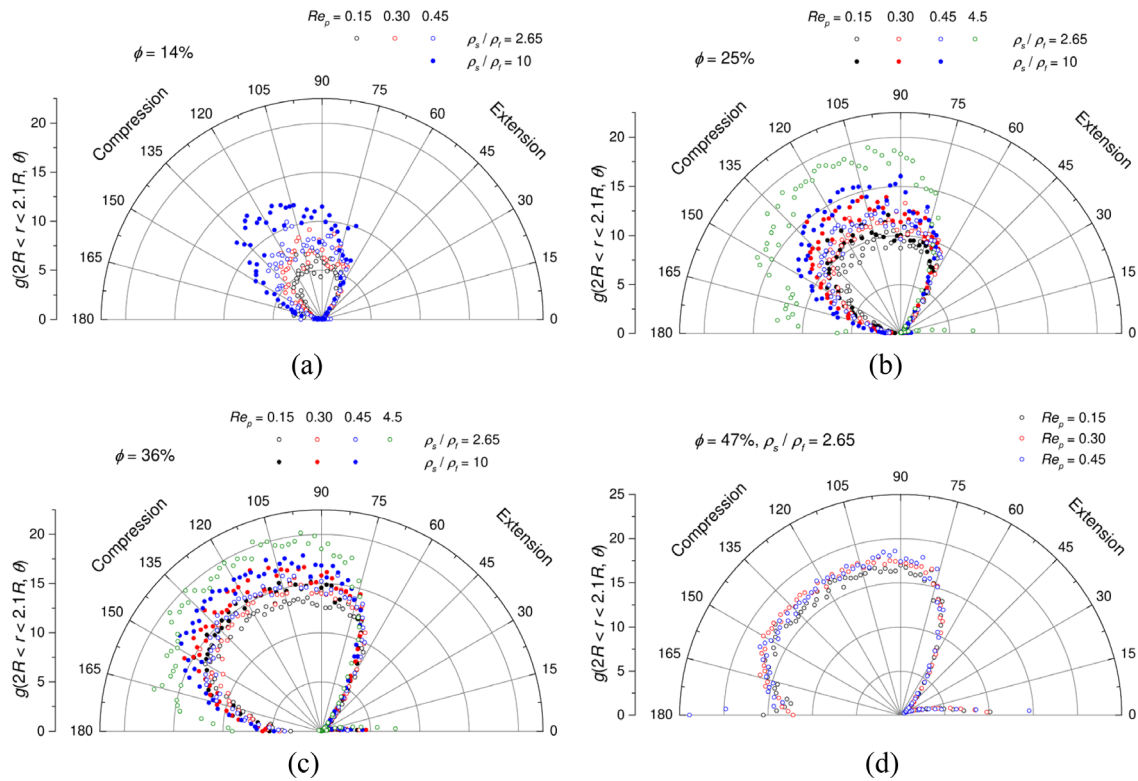


FIG. 25. Pair distribution function: (a) $\phi = 14\%$, (b) $\phi = 25\%$, (c) $\phi = 36\%$, and (d) $\phi = 47\%$ with varying Re_p and ρ_s/ρ_f for suspensions of circular grains.

for a given grain to encounter another one in the compression zone and along the shear direction ($\theta \approx 0^\circ$). The probabilities in the compression zone also increase with Re_p , especially at low ϕ . The effect of Re_p , however, diminishes with ϕ as seen from Fig. 25(d) that the pair distributions are close when Re_p increases from 0.15 to 0.45 at $\phi = 47\%$. To further explore the role of particle inertia, pair distribution functions for suspensions of different density ratios

($\rho_s/\rho_f = 2.65$ and 10) are also presented in Figs. 25(a)–25(c). Similar to the influence of Re_p , the increase of grain density magnifies the anisotropy in the pair microstructure and fore-aft asymmetry.

The influence of grain convexity is further examined. As seen from Fig. 26 that the chance to find a neighbor at around $2R$ in the compression zone is reduced with decreasing CV, which is especially evident when CV drops from 0.91 to 0.84. It is probably because of the additional excluded areas near contact due to grain concavities.

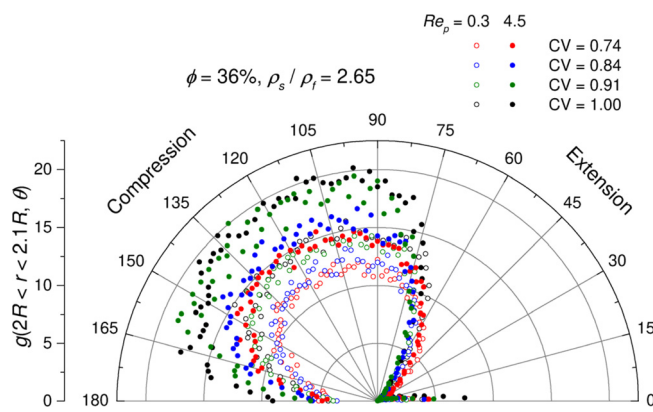


FIG. 26. Pair distribution function of $\phi = 36\%$ and $\rho_s/\rho_f = 2.65$ with varying Re_p and CV.

E. Grain rotation

Grain rotation plays an equally important role in the interactions among grains and between grains and fluid. The grain rotation is measured by Ω^* defined as the mean grain angular velocity Ω normalized by the bulk shear rate of the mixture, i.e., $\Omega^* = \Omega/\dot{\gamma}$.

For the results of circular grain suspensions presented in Fig. 27, Ω^* decreases with increasing ϕ for all Reynolds numbers, in agreement with previous studies.¹⁵ It can be understood that higher volume fraction leads to more significant constraints from neighbors on grain rotation. The comparisons between different grain density ρ_s for $\phi = 25\%$ and 36% show reduced grain rotation at higher ρ_s . Similarly, grain angular velocity declines as Reynolds number rises in accordance with that reported by Mikulencak and Morris⁶⁰ using data collected from the literature. It may be attributed to the enhanced inter-grain contacts at large Re_p that suppresses the shear-induced grain rotation.

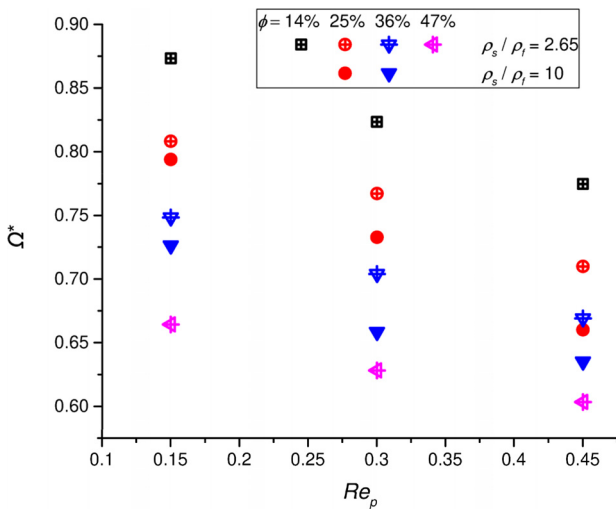


FIG. 27. Relationship between normalized mean grain angular velocity and Re_p at different ϕ and ρ_s/ρ_f for suspensions of circular grains.

The reduction in grain rotation at higher Re_p and ρ_s has resulted in the rise of shear stress or viscosity of the suspensions because of the steeper velocity gradients of interstitial fluid.²⁰

Figure 28 shows the normalized average grain rotation in suspensions with non-circular grains at $\phi = 36\%$ and $Re_p = 0.3$ and 4.5. Regardless of the particle Reynolds number, grain rotation decreases monotonically with both decreasing AR and CV although at different declining rates. The drop is faster with respect to decreasing AR and the trend is accelerating. Contrarily, a mild descent of grain rotation is observed with decreasing CV, especially when CV becomes smaller than 0.91, which is similar to the increasing trend of relative viscosity in Fig. 20(b). Moreover, the rate of descent is repressed by inertia which results in flatter curves when Re_p increases from 0.3 to 4.5.

Based on the above analyses, it can be concluded that grain shape has a significant impact on the viscosity of suspensions due to the interplay among inter-grain collisions, fluid-grain interactions, and

the non-uniform flow profiles. Grains with lower AR or CV tend to have a larger surface area and can, thus, intensify inter-grain and fluid-grain interactions. Specifically, concave grains increase the grain hydrodynamic stresslet by augmenting fluid-grain interactions. Contrarily, the grain hydrodynamics first increases with decreasing AR before declining, possibly because grains with lower AR are more likely to align with the flow direction. When the Reynolds stress becomes non-negligible, concave particles play a more significant role in perturbing the flow field while AR has less impact. Moreover, both AR and CV can suppress grain rotation, leading to higher shear stresses.

V. CONCLUSIONS

The rheology of 2D fluid-grain mixtures in a Couette flow has been studied using a fully resolved SPH-DEM method, with an emphasis on the roles of inertia and grain shape. The model has been rigorously validated through several benchmark problems, including water entry of a disk, sedimentation of an ellipse, periodic flow around a sunflower-shaped object, pair-disk trajectories in a shear flow, and the DKT phenomenon of two settling disks. The test results have adequately verified the accuracy of the present SPH-DEM method in simulating grain-fluid hydrodynamic interaction and inter-grain collision, as well as in dealing with complex grain shapes. The main findings from the study are summarized below.

- (1) In the macroscale, the suspension effective viscosity intensifies with increasing particle Reynolds number Re_p , solid concentration ϕ , and solid-to-fluid density ratio ρ_s/ρ_f , leading to more pronounced shear-thickening behavior. Additionally, suspensions of grains with lower AR and CV present greater effective viscosity.
- (2) The transitional behavior of suspensions is analyzed by separating the contributions to the bulk shear stress. It is found that the increase of effective viscosity is mainly attributable to the enhancement of fluid-grain hydrodynamic interaction, inter-grain collision, and Reynolds stress, whereas the contribution from fluid viscous stress remains largely unaltered with increasing Re_p , ϕ , and ρ_s/ρ_f . Additionally, the contribution of Reynolds stress magnifies when the inertia increases.

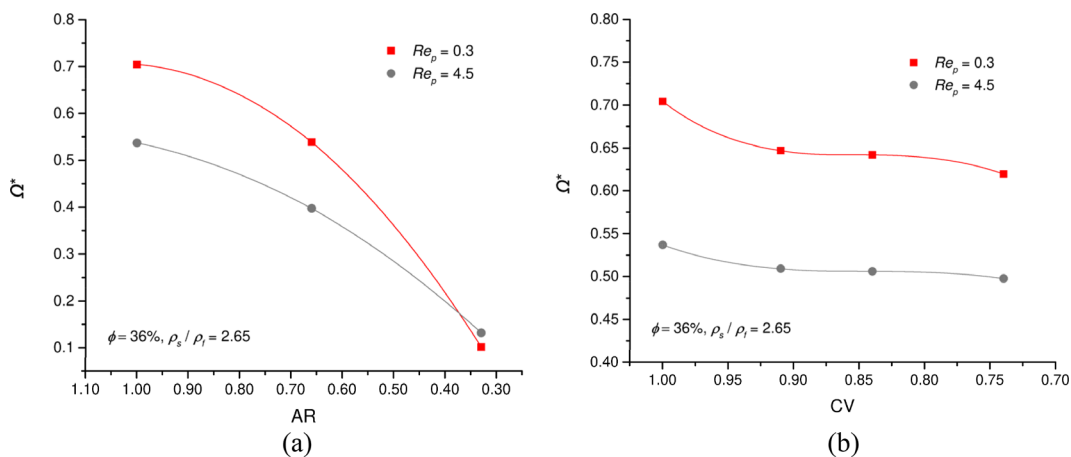


FIG. 28. Normalized mean grain angular velocity with different (a) aspect ratio and (b) convexity.

The elongation and concavity of suspended grains will also increase both the particle-fluid hydrodynamic and inter-grain collision contributions to the overall effective viscosity. The grain concavity will intensify the Reynolds stress when the inertial effect becomes nonnegligible.

- (3) Grain clustering is found near the walls in suspension flows. Inertia and grain elongation and concavity will increase the solid concentration near walls. As for near contact pair structures, the fore-aft symmetry breaks in the sheared suspension flow. Such asymmetry becomes more evident as Re_p , ϕ , or ρ_s increases or grain convexity decreases.
- (4) Average particle angular velocities show dependence on Re_p , ϕ , ρ_s , AR, and CV. Grain rotations are suppressed by increasing inertia and non-circular grain shapes. The microstructural anisotropy and grain kinematics characteristics play a crucial role in the shear-thickening behavior observed in noncolloidal suspension flows.

Although microscopic analyses are presented in the study, there is still a need for quantitative correlations between the macroscopic viscosity and microscopic quantities such as pair distribution, grain rotation, and grain shape. It is possible to develop such correlations by extending existing semi-empirical formulas (e.g., Eilers formula⁶¹), which will be explored in future studies.

ACKNOWLEDGMENTS

The study has been funded by the Key R&D Program of Zhejiang Province (No. 2022C03180), Zhejiang Provincial Natural Science Foundation of China (No. LR23E080001), Fundamental Research Funds for the Central Universities (No. 2021FZZX001-14), and ZJU-ZCCC Institute of Collaborative Innovation (No. ZDJG2021001).

AUTHOR DECLARATIONS

Conflict of Interest

The authors have no conflicts to disclose.

Author Contributions

Yueting Li: Conceptualization (equal); Data curation (equal); Formal analysis (equal); Investigation (equal); Software (equal); Validation (equal); Visualization (equal); Writing – original draft (equal). **Ning Guo:** Conceptualization (equal); Funding acquisition (equal); Methodology (equal); Project administration (equal); Resources (equal); Supervision (equal); Writing – review & editing (equal). **Zhongxuan Yang:** Conceptualization (equal); Funding acquisition (equal); Resources (equal); Writing – review & editing (equal). **Jidong Zhao:** Validation (equal); Writing – review & editing (equal).

DATA AVAILABILITY

The data that support the findings of this study are available within the article.

REFERENCES

- ¹D. Prasad and H. K. Kytömaa, “Particle stress and viscous compaction during shear of dense suspensions,” *Int. J. Multiphase Flow* **21**(5), 775–785 (1995).

- ²A. Sierou and J. F. Brady, “Rheology and microstructure in concentrated non-colloidal suspensions,” *J. Rheol.* **46**(5), 1031–1056 (2002).
- ³A. Sierou and J. F. Brady, “Shear-induced self-diffusion in non-colloidal suspensions,” *J. Fluid Mech.* **506**, 285–314 (2004).
- ⁴E. Nazockdast and J. F. Morris, “Pair-particle dynamics and microstructure in sheared colloidal suspensions: Simulation and Smoluchowski theory,” *Phys. Fluids* **25**(7), 070601 (2013).
- ⁵J. F. Morris and B. Katyal, “Microstructure from simulated Brownian suspension flows at large shear rate,” *Phys. Fluids* **14**(6), 1920–1937 (2002).
- ⁶J. F. Brady and J. F. Morris, “Microstructure of strongly sheared suspensions and its impact on rheology and diffusion,” *J. Fluid Mech.* **348**, 103–139 (1997).
- ⁷A. J. C. Ladd, “Numerical simulations of particulate suspensions via a discretized Boltzmann equation. Part 1. Theoretical foundation,” *J. Fluid Mech.* **271**, 285–309 (1994).
- ⁸A. J. C. Ladd, “Numerical simulations of particulate suspensions via a discretized Boltzmann equation. Part 2. Numerical results,” *J. Fluid Mech.* **271**, 311–339 (1994).
- ⁹A. J. C. Ladd and R. Verberg, “Lattice-Boltzmann simulations of particle-fluid suspensions,” *J. Stat. Phys.* **104**, 1191–1251 (2001).
- ¹⁰H. Haddadi and J. F. Morris, “Microstructure and rheology of finite inertia neutrally buoyant suspensions,” *J. Fluid Mech.* **749**, 431–459 (2014).
- ¹¹J. Kromkamp, D. van den Ende, D. Kandhai, R. van der Sman, and R. Boom, “Lattice Boltzmann simulation of 2D and 3D non-Brownian suspensions in Couette flow,” *Chem. Eng. Sci.* **61**(2), 858–873 (2006).
- ¹²J. Guo, Q. Zhou, and R. C.-K. Wong, “Effects of volume fraction and particle shape on the rheological properties of oblate spheroid suspensions,” *Phys. Fluids* **33**, 081703 (2021).
- ¹³G. Guan and J. Lin, “Study on the interaction and motion patterns of squirmers swimming in a shear flow,” *Phys. Fluids* **35**, 063302 (2023).
- ¹⁴F. Picano, W.-P. Breugem, and L. Brandt, “Turbulent channel flow of dense suspensions of neutrally buoyant spheres,” *J. Fluid Mech.* **764**, 463–487 (2015).
- ¹⁵D. Alghalibi, I. Lashgari, L. Brandt, and S. Hormozi, “Interface-resolved simulations of particle suspensions in Newtonian, shear thinning and shear thickening carrier fluids,” *J. Fluid Mech.* **852**, 329–357 (2018).
- ¹⁶S. Gallier, E. Lemaire, F. Peters, and L. Lobry, “Rheology of sheared suspensions of rough frictional particles,” *J. Fluid Mech.* **757**, 514–549 (2014).
- ¹⁷R. Glowinski, T. W. Pan, T. I. Hesla, D. D. Joseph, and J. Périaux, “A fictitious domain approach to the direct numerical simulation of incompressible viscous flow past moving rigid bodies: Application to particulate flow,” *J. Comput. Phys.* **169**(2), 363–426 (2001).
- ¹⁸M. Rahmani, A. Hammouti, and A. Wachs, “Momentum balance and stresses in a suspension of spherical particles in a plane Couette flow,” *Phys. Fluids* **30**, 043301 (2018).
- ¹⁹Y. Xia, Z. Yu, and Y. Guo, “Interface-resolved numerical simulations of particle-laden turbulent channel flows with spanwise rotation,” *Phys. Fluids* **32**, 013303 (2020).
- ²⁰N. A. Patankar and H. H. Hu, “Finite Reynolds number effect on the rheology of a dilute suspension of neutrally buoyant circular particles in a Newtonian fluid,” *Int. J. Multiphase Flow* **28**(3), 409–425 (2002).
- ²¹P. M. Kulkarni and J. F. Morris, “Suspension properties at finite Reynolds number from simulated shear flow,” *Phys. Fluids* **20**, 040602 (2008).
- ²²G. Zhou and A. Prosperetti, “Inertial effects in shear flow of a fluid-particle mixture: Resolved simulations,” *Phys. Rev. Fluids* **5**, 084301 (2020).
- ²³S. B. Lindström and T. Uesaka, “A numerical investigation of the rheology of sheared fiber suspensions,” *Phys. Fluids* **21**(8), 083301 (2009).
- ²⁴H. I. Andersson, E. Celledoni, L. Ohm, B. Owren, and B. K. Tapley, “An integral model based on slender body theory, with applications to curved rigid fibers,” *Phys. Fluids* **33**, 041904 (2021).
- ²⁵M. Blair and C. Ness, “Shear thickening in dense suspensions driven by particle interlocking,” *J. Fluid Mech.* **948**, A48 (2022).
- ²⁶R. Cai, H. Xiao, I. C. Christov, and Y. Zhao, “Diffusion of ellipsoidal granular particles in shear flow,” *AIChE J.* **67**(2), e17109 (2021).
- ²⁷M. Daghooghi and I. Borazjani, “The effects of irregular shape on the particle stress of dilute suspensions,” *J. Fluid Mech.* **839**, 663–692 (2018).
- ²⁸X. Bian, S. Litvinov, M. Ellero, and N. J. Wagner, “Hydrodynamic shear thickening of particulate suspension under confinement,” *J. Non-Newtonian Fluid Mech.* **213**, 39–49 (2014).

- ²⁹A. Vázquez-Quesada and M. Ellero, "Rheology and microstructure of non-colloidal suspensions under shear studied with smoothed particle hydrodynamics," *J. Non-Newtonian Fluid Mech.* **233**, 37–47 (2016).
- ³⁰R. B. Canelas, A. J. C. Crespo, J. M. Domínguez, R. M. L. Ferreira, and M. Gómez-Gesteira, "SPH-DCDEM model for arbitrary geometries in free surface solid–fluid flows," *Comput. Phys. Commun.* **202**, 131–140 (2016).
- ³¹H. Wendland, "Piecewise polynomial, positive definite and compactly supported radial functions of minimal degree," *Adv. Comput. Math.* **4**, 389–396 (1995).
- ³²J. Bonet and T.-S. L. Lok, "Variational and momentum preservation aspects of smooth particle hydrodynamic formulations," *Comput. Methods Appl. Mech. Eng.* **180**(1–2), 97–115 (1999).
- ³³J. P. Morris, P. J. Fox, and Y. Zhu, "Modeling low Reynolds number incompressible flows using SPH," *J. Comput. Phys.* **136**(1), 214–226 (1997).
- ³⁴H. Gotoh, T. Shibahara, and T. Sakai, "Sub-particle-scale turbulence model for the MPS method - Lagrangian flow model for hydraulic engineering," *Comput. Fluid Dyn. J.* **9**, 339–347 (2001).
- ³⁵D. Molteni and A. Colagrossi, "A simple procedure to improve the pressure evaluation in hydrodynamic context using the SPH," *Comput. Phys. Commun.* **180**(6), 861–872 (2009).
- ³⁶R. Vacondio, B. D. Rogers, P. K. Stansby, P. Mignosa, and J. Feldman, "Variable resolution for SPH: A dynamic particle coalescing and splitting scheme," *Comput. Methods Appl. Mech. Eng.* **256**, 132–148 (2013).
- ³⁷S. Koshizuka, A. Nobe, and Y. Oka, "Numerical analysis of breaking waves using the moving particle semi-implicit method," *Int. J. Numer. Methods Fluids* **26**(7), 751–769 (1998).
- ³⁸K. H. Hunt and F. R. E. Crossley, "Coefficient of restitution interpreted as damping in vibroimpact," *J. Appl. Mech.* **42**, 440–445 (1975).
- ³⁹S. Luding, "Introduction to discrete element methods," *Eur. J. Environ. Civil Eng.* **12**(7–8), 785–826 (2008).
- ⁴⁰D. F. Vetsch, "Numerical simulation of sediment transport with meshfree methods," Ph.D. thesis (ETH Zurich, 2012).
- ⁴¹M. Greenhow and W.-M. Lin, "Nonlinear free surface effects: Experiments and theory," Report No. 83-19, Massachusetts Institute of Technology, Department of Ocean Engineering, 1983.
- ⁴²X. Zhu, O. M. Faltinsen, and C. Hu, "Water entry and exit of a horizontal circular cylinder," *J. Offshore Mech. Arct. Eng.* **129**(4), 253–264 (2007).
- ⁴³Z. Xia, K. W. Connington, S. Rapaka, P. Yue, J. J. Feng, and S. Chen, "Flow patterns in the sedimentation of an elliptical particle," *J. Fluid Mech.* **625**, 249–272 (2009).
- ⁴⁴K. Suzuki and T. Inamura, "Effect of internal mass in the simulation of a moving body by the immersed boundary method," *Comput. Fluids* **49**(1), 173–187 (2011).
- ⁴⁵S. Khorasanizade and J. M. M. Sousa, "A two-dimensional segmented boundary algorithm for complex moving solid boundaries in Smoothed Particle Hydrodynamics," *Comput. Phys. Commun.* **200**, 66–75 (2016).
- ⁴⁶W. Pan, J. Bao, and A. M. Tartakovsky, "Smoothed particle hydrodynamics continuous boundary force method for Navier–Stokes equations subject to a Robin boundary condition," *J. Comput. Phys.* **259**, 242–259 (2014).
- ⁴⁷Y. J. Choi, M. A. Hulsen, and H. E. H. Meijer, "An extended finite element method for the simulation of particulate viscoelastic flows," *J. Non-Newtonian Fluid Mech.* **165**(11–12), 607–624 (2010).
- ⁴⁸M. Uhlmann, "An immersed boundary method with direct forcing for the simulation of particulate flows," *J. Comput. Phys.* **209**(2), 448–476 (2005).
- ⁴⁹R. A. Bagnold, "Experiments on a gravity-free dispersion of large solid spheres in a Newtonian fluid under shear," *Proc. R. Soc. A* **225**(1160), 49–63 (1954).
- ⁵⁰R. M. Iverson, "The physics of debris flows," *Rev. Geophys.* **35**(3), 245–296, <https://doi.org/10.1029/97RG00426> (1997).
- ⁵¹J. Yang and X. D. Luo, "Exploring the relationship between critical state and particle shape for granular materials," *J. Mech. Phys. Solids* **84**, 196–213 (2015).
- ⁵²M. K. Zarch, L. M. Zhang, S. M. Haeri, Z. D. Xu, and Z. X. Zeng, "Contributions of particle–fluid, collisional, and colloidal interactions to rheological behavior of soil–water mixtures," *J. Geotech. Geoenviron. Eng.* **148**(7), 04022053 (2022).
- ⁵³S. Mueller, E. W. Llewellyn, and H. M. Mader, "The rheology of suspensions of solid particles," *Proc. R. Soc. A* **466**(2116), 1201–1228 (2010).
- ⁵⁴T. N. Phung, J. F. Brady, and G. Bossis, "Stokesian dynamics simulation of Brownian suspensions," *J. Fluid Mech.* **313**, 181–207 (1996).
- ⁵⁵G. K. Batchelor, "The stress system in a suspension of force-free particles," *J. Fluid Mech.* **41**(3), 545–570 (1970).
- ⁵⁶N. A. Patankar, "Numerical simulation of particulate two-phase flow," Ph.D. thesis (University of Pennsylvania, 1997).
- ⁵⁷I. Lashgari, F. Picano, W.-P. Breugem, and L. Brandt, "Laminar, turbulent, and inertial shear-thickening regimes in channel flow of neutrally buoyant particle suspensions," *Phys. Rev. Lett.* **113**, 254502 (2014).
- ⁵⁸F. Picano, W.-P. Breugem, D. Mitra, and L. Brandt, "Shear thickening in non-Brownian suspensions: An excluded volume effect," *Phys. Rev. Lett.* **111**, 098302 (2013).
- ⁵⁹K. Yeo and M. R. Maxey, "Dynamics of concentrated suspensions of non-colloidal particles in Couette flow," *J. Fluid Mech.* **649**, 205–231 (2010).
- ⁶⁰D. R. Mikulencak and J. F. Morris, "Stationary shear flow around fixed and free bodies at finite Reynolds number," *J. Fluid Mech.* **520**, 215–242 (2004).
- ⁶¹J. J. Stickel and R. L. Powell, "Fluid mechanics and rheology of dense suspensions," *Annu. Rev. Fluid Mech.* **37**, 129–149 (2005).